Feasibility of MRI-only photon and proton dose calculations for pediatric patients with abdominal tumors

Guerreiro, Filipa; Koivula, Lauri; Seravalli, Enrica; Janssens, Geert O; Maduro, John H; Brouwer, Charlotte L; Korevaar, Erik W; Knopf, Antje-Christin; Korhonen, Juha; Raaymakers, Bas W

Published in:
Physics in Medicine and Biology

DOI:
10.1088/1361-6560/ab0095

Publication date:
2019

Physics in Medicine & Biology

PAPER

Feasibility of MRI-only photon and proton dose calculations for pediatric patients with abdominal tumors

To cite this article: Filipa Guerreiro *et al* 2019 *Phys. Med. Biol.* **64** 055010

IOP Publishing Phys. Med. Biol. 64 (2019) 055010 (13pp) https://doi.org/10.1088/1361-6560/ab0095

Physics in Medicine & Biology

IPEM Institute of Physics and Engineering in Medicine

PAPER

Feasibility of MRI-only photon and proton dose calculations for pediatric patients with abdominal tumors

RECEIVED
24 July 2018

REVISED
17 January 2019

ACCEPTED FOR PUBLICATION
22 January 2019

PUBLISHED
25 February 2019

Filipa Guerreiro[1], Lauri Koivula[2], Enrica Seravalli[1], Geert O Janssens[3], John H Maduro[4], Charlotte L Brouwer[4], Erik W Korevaar[4], Antje C Knopf[4], Juha Korhonen[5,6] and Bas W Raaymakers[1]

[1] Department of Radiotherapy, University Medical Center Utrecht, Utrecht, The Netherlands
[2] Department of Radiation Oncology, Cancer Center, Helsinki University Hospital, Helsinki, Finland
[3] Department of Radiation Oncology, University Medical Center Utrecht, Utrecht, The Netherlands
[4] Department of Radiation Oncology, University Medical Center Groningen, University of Groningen, Groningen, The Netherlands
[5] Department of Medical Imaging and Radiation Therapy, Kymenlaakso Central Hospital, Kymenlaakso Social and Health Services (Carea), Kotka, Finland
[6] Department of Electrical Engineering and Automation, Health Technology, Aalto University, Espoo, Finland

E-mail: f.guerreiro@umcutrecht.nl

Keywords: magnetic resonance imaging, MRI-only treatment planning, pediatric IGRT, abdominal cancer, synthetic CT, proton therapy, photon therapy

Abstract

The purpose of this study was to develop a method enabling synthetic computed tomography (sCT) generation of the whole abdomen using magnetic resonance imaging (MRI) scans of pediatric patients with abdominal tumors. The proposed method relies on an automatic atlas-based segmentation of bone and lungs followed by an MRI intensity to synthetic Hounsfield unit conversion. Separate conversion algorithms were used for bone, lungs and soft-tissue. Rigidly registered CT and T2-weighted MR images of 30 patients in treatment position and with the same field of view were used for the evaluation of the atlas and the conversion algorithms. The dose calculation accuracy of the generated sCTs was verified for volumetric modulated arc therapy (VMAT) and pencil beam scanning (PBS). VMAT and PBS plans were robust optimized on an internal target volume (ITV) against a patient set-up uncertainty of 5 mm. Average differences between CT and sCT dose calculations for the ITV $V_{95\%}$ were 0.5% (min 0.0%; max 5.0%) and 0.0% (min −0.1%; max 0.1%) for VMAT and PBS dose distributions, respectively. Average differences for the mean dose to the organs at risk were <0.2% (min −0.6%; max 1.2%) and <0.2% (min −2.0%; max 2.6%) for VMAT and PBS dose distributions, respectively. Results show that MRI-only photon and proton dose calculations are feasible for children with abdominal tumors.

1. Introduction

Wilms' tumor (WT) and neuroblastoma (NBL) belong to the most frequent abdominal tumors in pediatric patients. By combining the use of surgery, chemotherapy and radiotherapy, the survival rates for these patients have increased over the past few decades up to 90% for WT and 60% for NBL (Pritchard-Jones *et al* 2015, Ladenstein *et al* 2017).

During radiotherapy treatment planning (RTP) with either photons or protons, computed tomography (CT) imaging is used for the conversion of Hounsfield unit (HU) values to relative electron density (in photon therapy) or stopping power ratio relative to water (in proton therapy). This information is needed for the computation of the dose to deliver to the patient (Chernak *et al* 1975). Magnetic resonance imaging (MRI) yields superior soft-tissue visualization allowing for a better visualization of the target and the assessment of organs at risk (OARs) motion and deformation without patient radiation burden (Lagendijk *et al* 2014). In the last few years, MRI-only RTP has been introduced into clinics (Edmund and Nyholm 2017, Tenhunen *et al* 2018) promising to avoid systematic uncertainties arising from the CT-MR image registration and to decrease the patient exposure to ionizing radiation by skipping the planning-CT. Reducing both the registration uncertainties and

the patient imaging dose is particularly important for pediatric patients for whom the radiation oncology community strives to minimize the risk of radiation-induced complications.

Currently, the main challenge of performing MRI-only dose calculations is the estimation of tissue attenuation properties from the MR images. For this purpose, the commonly named pseudo-CT or synthetic-CT (sCT) images can be generated from the patient's MRI to serve as surrogate for the dose calculations.

Two recent review articles by Edmund and Nyholm (2017) and Johnstone *et al* (2018) provide a comprehensive overview of the currently available sCT generation methods. These can be divided in four different approaches: bulk-density override, atlas-based, voxel-based and more recently introduced deep learning methods. Bulk-density override has been studied for over a decade with either manual or automatic contour segmentation (Lee *et al* 2003, Stanescu *et al* 2008). Although this technique provides a user-friendly method for sCT generation, it does not allow a straightforward creation of reference images for patient positioning verification during treatment (Johnstone *et al* 2018). For the atlas-based methods, the main goal is to create an MR to CT image atlas and convert the MRI intensity into HU values by registering the patient's MRI to the atlas (Dowling *et al* 2012, 2015, Uh *et al* 2014, Guerreiro *et al* 2017). The main drawbacks of this method are the lack of adaptation to atypical anatomies and the strict requirements for imaging posture and settings. Voxel-based methods rely only on the MRI contrast, independently of the voxels location, for the generation of sCT images for different body parts and anatomies (Hsu *et al* 2013, Edmund *et al* 2014, Korhonen *et al* 2014, Jonsson *et al* 2015). Compared to the atlas-based approach, this method is more vulnerable to MRI artifacts (Sjolund *et al* 2015). More recently, novel techniques for sCT generation are being explored by deep learning methods. Han (2017) and Dinkla *et al* (2018) have presented fast sCT generation methods using a convolutional neural network (CNN) and Maspero *et al* (2018) using a conditional generative adversarial network (cGAN). Despite providing acceptable dose calculation accuracy, none of these sCT generation approaches is reported to outperform the others (Edmund and Nyholm 2017, Johnstone *et al* 2018). Moreover, a population-based study comparing CT- and sCT-based dose calculations should be initiated in order to establish acceptable dosimetric deviations from the planning-CT dose for clinically relevant dose volume histogram (DVH) parameters (Korsholm *et al* 2014).

In the past few years using the mentioned techniques, sCT images have been generated for several body sites such as brain (Edmund *et al* 2014, Jonsson *et al* 2015, Koivula *et al* 2016, Dinkla *et al* 2018), head & neck (Hsu *et al* 2013, Sjolund *et al* 2015, Guerreiro *et al* 2017) and pelvis (Korhonen *et al* 2014, Koivula *et al* 2016, Guerreiro *et al* 2017, Maspero *et al* 2017, 2018) in adult patients. The purpose of this study was to develop a method enabling sCT generation for pediatric patients, which is one of the most challenging patient populations as a result of the highly individual anatomies among patients. To the author's knowledge, the present work is the first generating sCTs with a large field of view (FOV), including the whole abdomen, for children diagnosed with abdominal cancer. The presented sCT generation method was based on an automatic atlas-based segmentation of tissue classes followed by a voxel-based MRI intensity to HU values conversion algorithm. The accuracy of performing dose calculations with the generated sCTs was assessed for both photon and proton irradiation modalities.

2. Material and methods

2.1. Patient and imaging characteristics

After institutional review board approval (WAG/mb/17/008865), data from 30 consecutive patients treated at the Department of Radiotherapy of University Medical Center Utrecht (UMCU) between April 2015 and January 2018 were included in this study: 9 WT patients (mean age: 3, range: 2–4 years), undergoing flank irradiation, and 21 NBL patients (mean age: 4, range 2–7 years). For 9 out of 30 patients, the target was located on the upper part of the abdomen within the diaphragm border (Pat_{upp}s), while for the remaining 21 patients the target was located on the lower part of the abdomen (Pat_{low}s).

After chemotherapy and resection, all patients received radiotherapy to the primary tumor site. For treatment preparation, 4-dimensional CT (4D-CT) and T2-weighted (T2w-) MR images were acquired for each patient on the same day ($\leqslant$45 min), in radiotherapy treatment position and using the same FOV which covered the whole abdomen of the patient: from the neck until the pelvis. Patients were fixated in a supine position in an individualized vacuum mattress (Bluebag, Elekta, Stockholm, Sweden) and imaging was performed with patients under general anesthesia. The 4D-CT images were acquired using a 16-, 40-, or 64-channel detector scanner (Brilliance, Philips Medical Systems, Best, The Netherlands). Respiratory trace measurements for pulmonary gating were obtained using a deformable rubber belt fixed to the patient's chest (Philips Bellow System, Philips Medical Systems, Best, The Netherlands). The planning-CT was obtained by taking the pixel-by-pixel mean of the ten phases of the 4D-CT. Voxel dimensions ranged between 0.8–1.4 mm for both left-right (LR) and anterior–posterior (AP) directions and between 2–3 mm for the cranio-caudal (CC) direction, depending on the patient. The T2w-MR images were acquired using a 1.5T Philips Achieva MR scanner (Philips Medical Systems, Best, The Netherlands) and a 3D turbo spin echo sequence without motion compensation strategies. Voxel dimensions ranged between 0.7–0.8 mm for both LR and CC directions and between 1–3 mm for the AP direction, depend-

ing on the patient. The specific sequence parameters for the T2w-MR images were as follows: TE = 90 ms, TR = 454.4 ms, flip angle = 90°, BW = 570 Hz and acquisition duration = 249 s.

2.2. sCT generation

The proposed sCT method is an extension of the previously published dual-model technique, described in detail in Korhonen *et al* (2014) and Koivula *et al* (2016, 2017), combining an automatic atlas-based segmentation and a voxel-based MRI intensity to HU values conversion algorithm for bone and soft-tissue classes. Briefly in the current sCT method, auto-segmentation and conversion algorithms for the lungs were included in addition to bone and soft-tissue classes. For each patient, a single T2w-MR image was used for the sCT generation. A schematic representation of the adopted workflow is shown in figure 1 and all steps are described in more detail on the following sections.

2.2.1. Automatic atlas-based segmentation

Rigidly registered, based on mutual information, planning-CT and T2w-MR images were used for the atlas construction. A selection of patients (24/30) was divided into three groups based on their height: group 1 (86–95 cm), group 2 (96–112 cm), and group 3 (113–124 cm), each group containing eight patients. A separate atlas was created for each of the three groups by manually contouring bones and lungs volumes on the T2w-MR images. For the sCT generation, the automatic segmentation of bone and lungs volumes from MRI was made using a leave-one-out strategy for the 24 patients included in the atlas database. For the remaining six patients, bone and lungs were automatically segmented using one of the three generated atlases depending on the patient's height. The commercial medical image processing software MIM (version 6.7, MIM Software, Inc., Cleveland, OH, USA) was used for the automatic atlas-based segmentation by creating a deformable registration based on mutual information between the patient's MR and the MR images in the atlas. Manually contoured bone and lungs volumes from the patients in the atlas were combined and average volumes were obtained for each patient. Additionally, the soft-tissue was automatically segmented using a Boolean exclusion of the segmented bone and lungs volumes from the body contour defined on the MRI. On the planning-CT, tissue classes were automatically segmented by applying a threshold: bone (HU $>$ 150), lungs (HU $<$ −150) and soft-tissue (−150 $<$ HU $<$ 150). No manual adjustments of the MRI and planning-CT contours were done after auto-segmentation.

2.2.2. Conversion algorithms for bone, lungs and soft-tissue

Before performing the MRI intensity to HU values conversion, the MR images were 3D bias-field corrected (Tustison *et al* 2010) to enable a uniform intensity level across the patient body. In addition, the original MRI intensity values were scaled to a coherent base level, which corresponded to the median intensity level of the adipose tissue calculated from the MR images of the 24 patients included in the atlases (Koivula *et al* 2017). This workflow was previously shown to be robust for the sCT generation using MRIs from multiple MR scanners and with different intensity levels.

The conversion from MRI intensity to HU values was done directly by using three different curves corresponding to each of the automatic segmented tissue classes (section 2.2.1): bone, lungs and soft-tissue. Conversion curves (figure 1) were constructed using the segmented CT and MRI volumes of the 24 patients included in the atlases. Furthermore, the three calculated conversion curves were used for the MRI intensity to HU values conversion for all 30 patients.

For the bone and lungs conversion curves construction, the MRI intensity and corresponding CT HU values were matched using histogram points: histogram peak as the median value and the 5% cut-off value from the median as minimum and maximum values. For the bone, the HU values conversion was executed as inversely proportional to the MRI intensity values. As a result, the low signal from cortical bone on the MRI was linked to high HU values (HU = 807) while the high signal from bone marrow on the MRI was linked to lower HU values (HU = −47). For the lungs, the MRI intensity to HU values correspondence was defined to be directly proportional. Therefore, the low signal from alveonic-rich tissue on the MRI was represented by low HU values (HU = −783) while the high signal from lung capillaries on the MRI was represented by higher HU values (HU = −101). For both conversion curves, a step-wise function using twelve constant HU segments was used to estimate the values in between. For the soft-tissue conversion curve construction, MRI intensity values were collected using regions of interest inserted in the muscle, adipose tissue and fluids. Then, the MRI values were converted into HU values in a three-part step-wise conversion relying on the known HUs of muscle (HU = 55), adipose tissue (HU = −105) and fluids (HU = 10). HU values between these three segments were interpolated using a step-wise function with three steps.

2.2.3. sCT image processing

For each patient, the sCT was re-sampled to the planning-CT dimensions. On the sCT, the body contour from the planning-CT was used instead of the body contour provided by the MRI. This was done to minimize

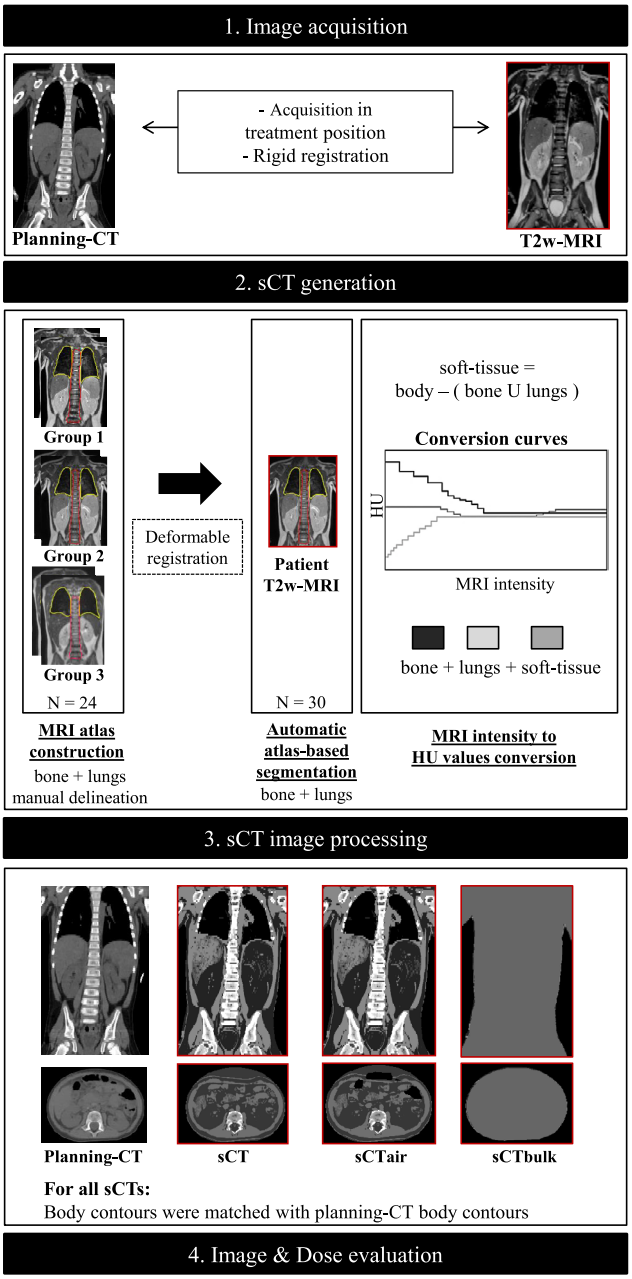

Figure 1. Schematic representation of the workflow used in this study. For the image acquisition (1), both planning-CT and T2w-MR images were acquired on the same day and in radiotherapy treatment position. The sCT generation method (2) is divided in two steps: the automatic atlas-based segmentation followed by the MRI intensity to HU values conversion for the bone, lungs and soft-tissue classes. For the atlas construction, image data of 24 out of 30 patients was used and divided into three groups according to the patient height. For each patient ($N = 30$), a single T2w-MR image was used for the sCT generation. The final two steps consisted of the sCT image processing (3) and the image and dose evaluation (4).

uncertainties arising from set-up and time differences between the CT and MR imaging sessions. Thus, areas of the MRI outside the planning-CT body contour were manually labeled as −1000 HU and areas of the planning-CT outside the MRI body contour were manually labeled as 0 HU. Furthermore, on the original sCTs the bowel gases were assigned automatically as muscle HU while no density override was performed on the planning-CT. To minimize the possible differences between the planning-CT and the original sCT doses arising from the bowel filling, a second set of sCTs was generated containing the air pockets extracted from the planning-CT (sCT_{air}).

2.3. Treatment planning characteristics

For both patient groups, the gross tumor volume (GTV) consisted of the pre-operative tumor extension, including pathologic lymph nodes and residual disease if applicable. The clinical target volume (CTV) was created by expanding the GTV by 5 to 10 mm, depending on the patient. To account for the breathing motion, assessed by using a 4D-CT and surgical clips as surrogates, an internal target volume (ITV) was individualized in each orthogonal direction for all patients.

The sCT dosimetric accuracy was assessed for both photon therapy with volumetric modulated arc therapy (VMAT), used currently clinically at the Department of Radiotherapy of UMCU to treat these patients, and proton therapy with pencil beam scanning (PBS). For both VMAT and PBS treatment plans, RTP was performed in RayStation treatment planning system (Raysearch, Stockholm, Sweden) using the planning-CT and a uniform dose grid of 3 mm. According to the clinical protocol, the VMAT plans consisted of a 6 MV full-arc. Since the target volumes are mainly located in the posterior part of the abdomen, the PBS plans were based on two or three posterior irradiation fields to avoid the effect of bowel filling on the dose distributions. The center of the ITV was selected as the isocenter for both delivery techniques. The prescribed dose (PD) ranged from 14.4 to 36.0 Gy, depending on the patient. To reduce the risk of asymmetric skeletal growth, a homogeneous dose was aimed for the vertebra volume adjacent to the ITV. To achieve that, the following constraint was implemented to the vertebra volume: $V_{70\%–80\%} > 95\%–98\%$, depending on the patient.

Both VMAT and PBS plans were robust optimized on the ITV using a minimax optimization method (Fredriksson *et al* 2011, RaySearch Laboratories 2014) and a uniform 5 mm patient set-up uncertainty. For the PBS plans, robustness against range uncertainty was not accounted for to assess the dose differences in a setting more susceptible to density changes between the planning-CT and the generated sCTs. For the robust plan optimization, plans were optimized accounting for the nominal plan plus 6 different scenarios where the plan isocenter was shifted in fixed directions using the magnitude of the selected set-up uncertainty (Fredriksson *et al* 2011, RayStation Laboratories 2014). For the plan robustness evaluation, dose distributions for different scenarios were computed using the same magnitude of the set-up uncertainty in 26 fixed directions. Additionally, the information from all 26 scenarios per technique was combined in a voxel-wise minimum evaluation dose (Vw_{min}) by calculating the minimal dose per voxel in all scenarios. Plans were considered robust if in the Vw_{min} 98% of the ITV received at least 95% of the PD ($V_{95\%} > 98\%$) (Korevaar *et al* 2017).

2.4. sCT evaluation

2.4.1. Image evaluation

The imaging evaluation of the original sCTs was done by calculating the voxel-wise mean error (ME) and the mean absolute error (MAE) in terms of HU against the corresponding planning-CT. The ME and MAE were calculated in a Boolean intersect of the automatic planning-CT and MRI bone, lungs, and soft-tissue volumes (section 2.2.1) to minimize the unavoidable HU differences due to random air pockets, posture and/or lungs volume differences due to breathing motion between consecutive CT and MR imaging sessions. In addition, the Dice similarity coefficient (DSC) was calculated for the segmented bone and lungs volumes on the planning-CT and MR images.

2.4.2. Dose evaluation

To validate the dosimetric accuracy of the sCTs, dose re-calculations of the VMAT and PBS plans were performed on the generated sCTs (sCT and sCT_{air}) and on a water bulk density sCT (sCT_{bulk}). The relative differences between the planning-CT and sCTs dose distributions were calculated for the following DVH metrics: ITV $D_{98\%}$, $D_{50\%}$, $D_{2\%}$ and $V_{95\%}$, as well as OARs (kidneys, liver, spleen) mean dose (D_{mean}), $D_{50\%}$, $D_{20\%}$ and $D_{2\%}$. Moreover, the dose distributions of the treatment plans re-calculated on all sCTs were compared to that on the planning-CT by means of different 3D global gamma criteria: (3%, 3 mm) and (2%, 2 mm), with a 90%, 50% and 10% dose threshold.

3. Results

3.1. Image evaluation

Coronal and sagittal slices of the planning-CT, T2w-MRI and the original sCT are shown in figure 2 for one Pat_{upp} (a)–(c) and one Pat_{low} (d)–(f). Automatic atlas-based segmentation time was approximately 3 min and MRI intensity to HU values conversion time was approximately 15 s per patient using a standard octa-core desktop computer with a 16 GB of RAM. Despite the fact that images were acquired on the same day and under radiotherapy treatment position, the planning-CT and MR images demonstrate substantial inter-scan differences regarding either the size of the patient, the lungs volume and the presence of air pockets (figures 2 and 3). Nevertheless, the original sCTs reproduced the appearance of the different tissue classes. The computed mean DSC was 0.90 ± 0.04 (min 0.82; max 0.98) and 0.74 ± 0.08 (min 0.54; max 0.87) for the bone and lungs volumes. The calculated ME was 11 ± 113 HU (min −170 HU; max 207 HU) in bone, -3 ± 65 HU (min −165 HU; max 163 HU) in lungs and 21 ± 11 HU (min 0 HU; max 55 HU) in soft-tissue. The calculated MAE was 212 ± 40 HU (min 154 HU; max 291 HU) in bone, 125 ± 24 HU (min 86 HU; max 198 HU) in lungs and 53 ± 7 HU (min 42 HU; max 74 HU) in soft-tissue. The largest HU discrepancies between the planning-CT and the original sCT images were seen in the lungs and in the ribs (figures 3(d) and (h)).

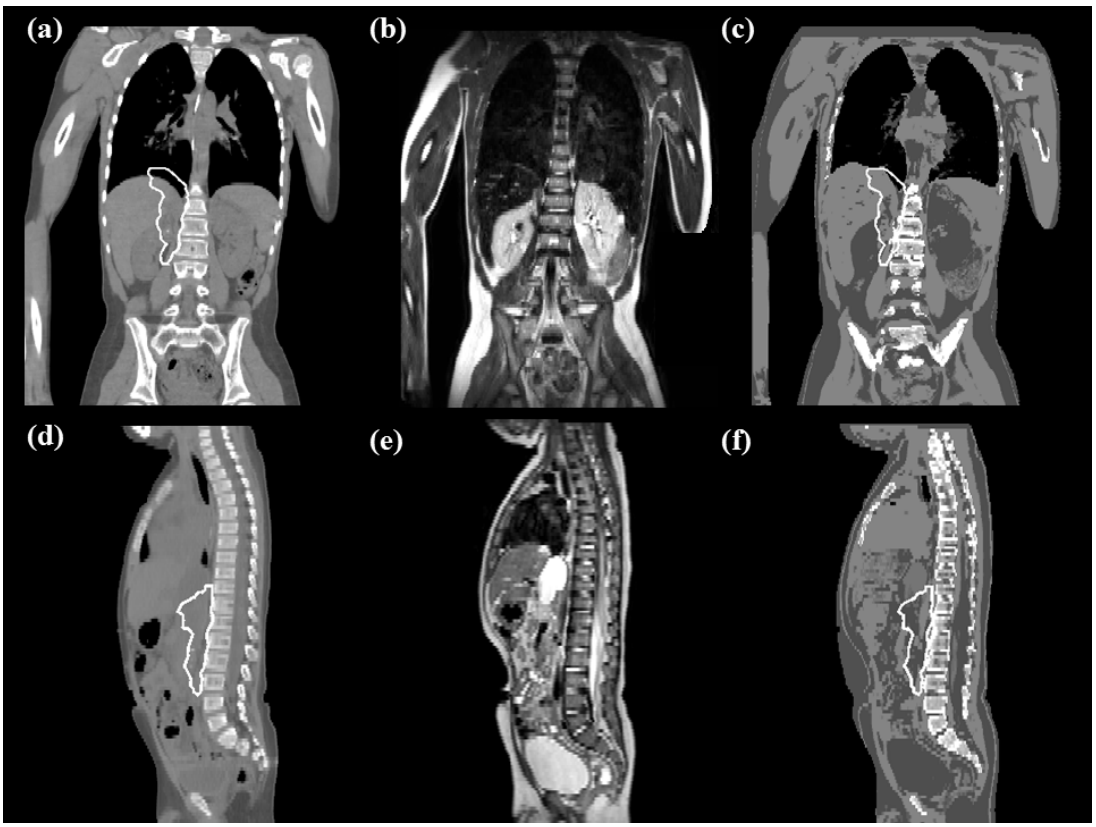

Figure 2. Coronal (top) and sagittal (bottom) slices of the planning-CT (a) (d), T2w-MRI (b) (e) and the original sCT (c) (f) for one Pat_{upp} (top) and one Pat_{low} (bottom). The ITV is denoted in white.

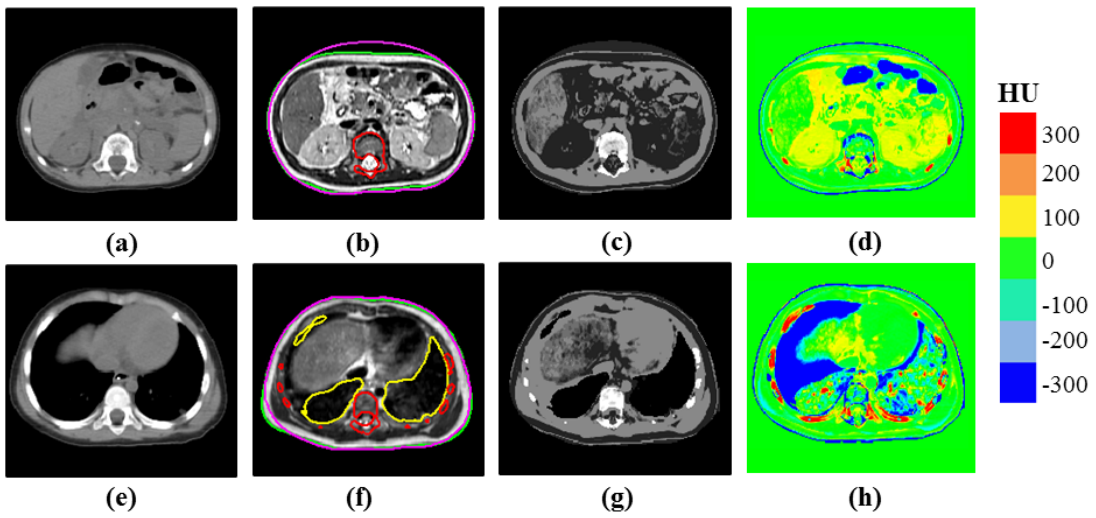

Figure 3. Transversal slices of the planning-CT (a) (e), T2w-MRI (b) (f) and the original sCT (c) (g) for one example patient. Body contours extracted from the planning-CT and MR images are presented in pink and green, respectively. The automatic atlas-based MRI contours for the bone and lungs are represented in red and yellow, respectively. HU differences between the planning-CT and the original sCT images are represented in (d) and (h).

3.2. Dose evaluation

Relative dose differences of clinically relevant DVH parameters between the planning-CT and all sCT dose distributions are illustrated using box-and-whisker plots in figure 4 for the ITV and in figure 5 for the OARs. Gamma pass-rates obtained between the planning-CT and all sCT dose distributions are given in table 1.

For the ITV, mean $V_{95\%}$ deviations to the planning-CT doses were 0.5% ± 1.4% (min 0.0%; max 5.0%) and 0.0% ± 0.0% (min 0.0%; max 0.1%) for the VMAT dose distributions re-calculated on the original sCTs and sCT_{air}s, respectively. For the PBS dose distributions, mean $V_{95\%}$ deviations were 0.0% ± 0.0% (min −0.1%; max 0.1%) and 0.0% ± 0.0% (min −0.1%; max 0.0%) for the original sCTs and sCT_{air}s, respectively. Larger dosimet-

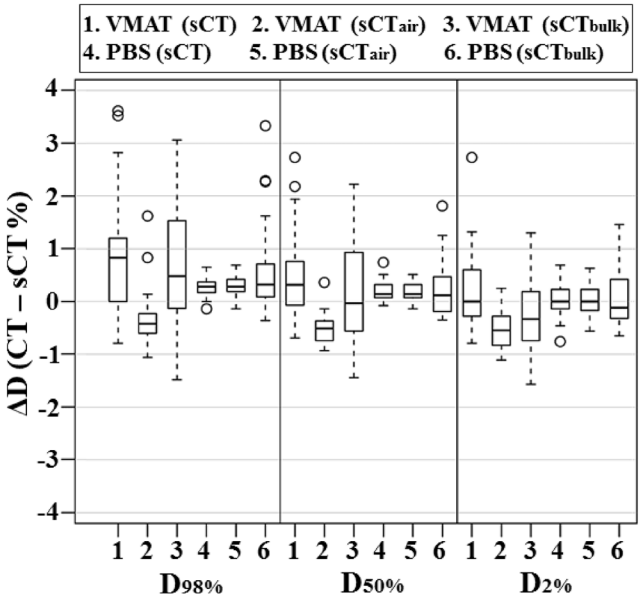

Figure 4. Box-and-whiskers plots of the ITV DVH parameters differences between the planning-CT and sCT dose distributions for the VMAT (1)–(3) and PBS (4)–(6) plans re-calculated on the original sCT (1) (4), sCT_{air} (2) (5) and sCT_{bulk} (3) (6). Values are presented as a percentage of the respective PD.

ric differences were observed between the planning-CT and the original sCT for the VMAT dose distributions (figure 4). The ITV coverage ($V_{95\%} > 99\%$) was not met for three patients due to the presence of large air pockets in the proximity of the ITV on the planning-CT and not on the sCT (figure 6). When inserting the air pockets from the planning-CT on the sCT_{air}, the ITV dosimetric differences were considerably reduced (figures 4 and 6). Given the use of posterior irradiation fields in the PBS plans, similar results were seen for the dose distributions re-calculated on both sCTs and sCT_{air}s (figures 4 and 6).

For the OAR, the D_{mean} differences ranged between (min −0.6%; max 1.2%) and (min −0.7%; max 0.1%) for the VMAT dose distributions re-calculated on the original sCTs and sCT_{air}s, respectively. For the PBS dose distributions, larger individual differences between the planning-CT and sCT were observed (figure 5). The range of D_{mean} differences was (min −2.0%; max 2.6%) and (min −2.6%; max 2.5%) for the original sCT and sCT_{air}, respectively. Furthermore, an increase up to 4% on the OAR $D_{2\%}$ was calculated for both delivery techniques for the Pat_{upp}s in comparison to the Pat_{low}s (table 2). This was due to the large inter-scan differences seen regarding the lungs volume definition between the planning-CT and MR images (figure 3).

Mean gamma pass-rates were above 87% for the generated sCTs independently of the considered gamma criteria. Focusing on the high-dose region (with a 90% dose cut-off), mean gamma pass-rates above 92% were achieved for both irradiation techniques. For the VMAT dose distributions re-calculated on the original sCTs, the gamma pass-rates were lower than for the sCT_{air}s due to the difference of air volumes on the planning-CT and sCT, as mentioned previously. When inserting the air pockets from the planning-CT on the sCT_{air}, the gamma pass-rates were considerably increased (table 1). For the PBS dose distributions, similar gamma pass-rates were obtained between the sCTs and sCT_{air}s. Moreover, large differences on the gamma pass-rates were denoted for the original sCTs between the Pat_{upp}s and Pat_{low}s (table 2). A decrease on the mean gamma pass-rates of 22 percentage points (pp) and 7 pp was observed for the Pat_{upp}s in comparison to Pat_{low}s for the VMAT and PBS dose distributions, respectively.

Furthermore, the dosimetric accuracy of the sCT_{bulk}s was reduced in comparison to performing the dose re-calculations on the generated sCTs, especially for the PBS dose distributions. For the VMAT dose distributions, mean DVH differences to the planning-CT doses were up to 0.8% (max 5.0%) versus 0.6% (max 1.6%) versus 0.7% (max 3.1%) for the sCT, sCT_{air} and sCT_{bulk}, respectively. For the PBS dose distributions, mean DVH differences were up to 0.5% (max 5.4%) versus 0.7% (max 5.3%) versus 4% (max 19.8%) for the sCT, sCT_{air} and sCT_{bulk}, respectively. Moreover, mean gamma pass-rates for the sCT_{bulk}s were considerably lower than for the generated sCTs, especially for the PBS dose distributions (table 1, <89%; min 53%). An increase on the mean gamma pass-rates up to 6 pp and 15 pp was achieved when using the generated sCTs in comparison to the sCT_{bulk}s for the VMAT and PBS dose re-calculations, respectively.

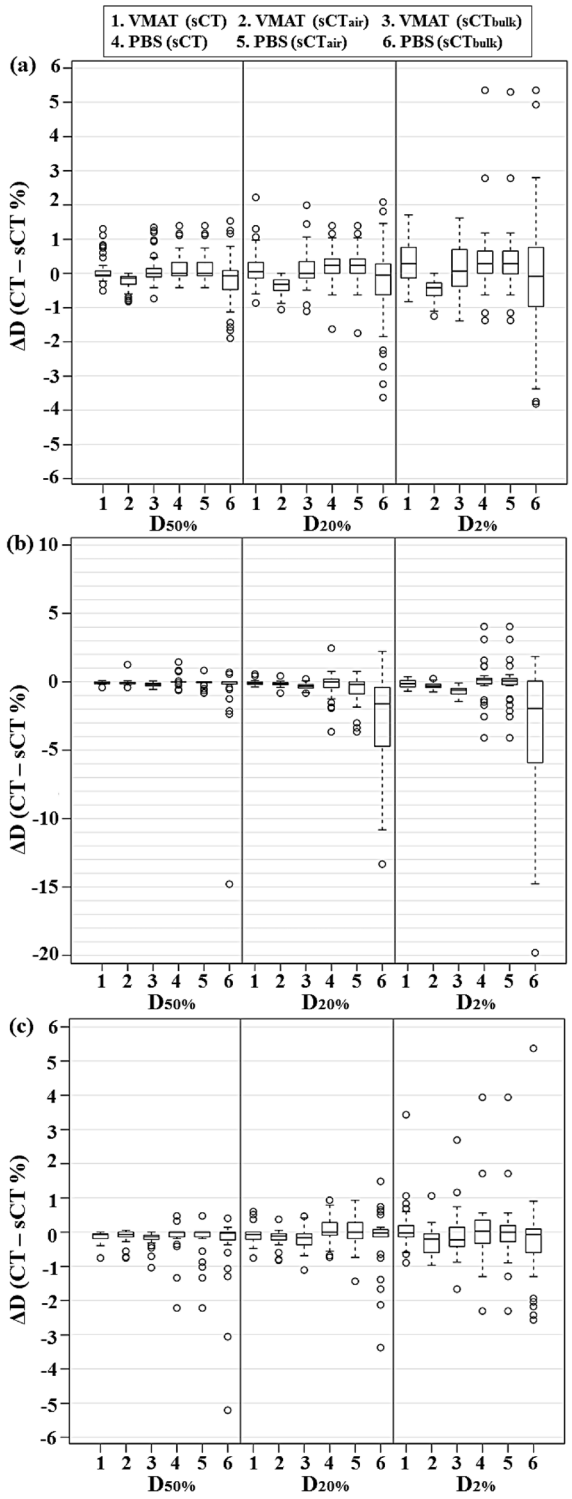

Figure 5. Box-and-whiskers plots of the kidneys (a), liver (b) and spleen (c) DVH dosimetric differences at a given relative volume between the planning-CT and the original sCT (1) (4), sCT_{air} (2) (5) and sCT_{bulk} (3) (6) for both VMAT (1)–(3) and PBS (4)–(6) dose distributions. Values are presented as a percentage of the respective PD.

4. Discussion

In this study, a method able to generate sCTs for the whole abdomen of pediatric patients using an automatic atlas-based segmentation combined with a triple-model technique for MRI intensity to HU values conversion was presented. To the author's knowledge, the present study is the first evaluating the feasibility of generating sCTs for children aged from 2 to 7 years old and treated for abdominal cancer, which is one of the most challenging patient populations as a result of the highly individual anatomies among patients. Results show that MRI-only photon and proton dose calculations on the generated sCTs were feasible.

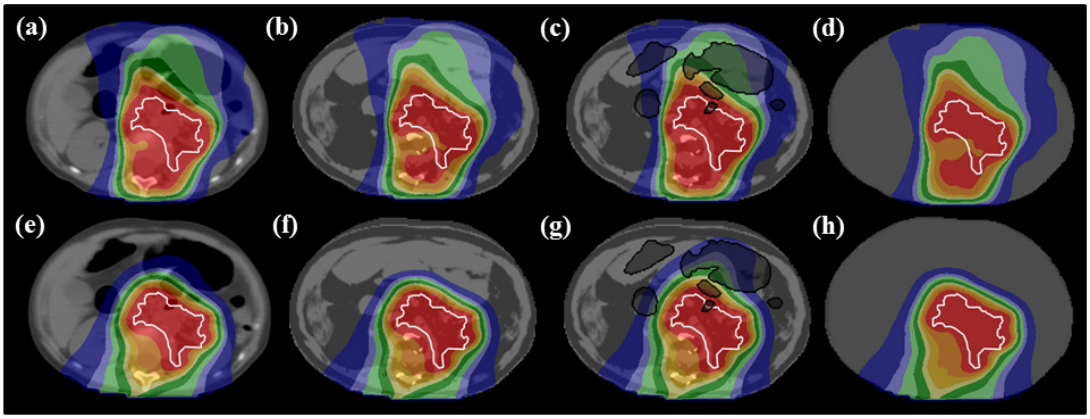

Figure 6. VMAT (top row) and PBS (bottom row) dose maps for dose distributions re-calculated on the planning-CT (a) (e), sCT (b) (f), sCT_{air} (c) (g) and sCT_{bulk} (d) (h) for one Pat_{low}. The ITV contour is represented in white. The PD is 21.6 Gy and the 95%PD isoline is shown in red.

Table 1. Percentage of gamma pass-rates (%) for the comparison of planning-CT and sCT doses using different gamma criteria (mm_%) and dose thresholds (10%, 50% and 90%).

			Gamma pass-rate (CT & sCT) (%)					
			10%		50%		90%	
Criteria	Dose		Mean + sd	Range	Mean + sd	Range	Mean + sd	Range
3 mm_3%	VMAT	sCT	99.3 ± 0.7	(97.2–99.9)	97.6 ± 3.3	(86.0–99.9)	97.6 ± 6.1	(74.8–100)
		sCT_{air}	99.5 ± 0.4	(98.8–99.9)	98.8 ± 1.2	(95.3–99.9)	99.6 ± 1.7	(91.6–100)
		sCT_{bulk}	99.1 ± 0.9	(96.2–99.8)	97.3 ± 2.9	(88.0–99.9)	98.0 ± 4.4	(84.2–100)
	PBS	sCT	91.4 ± 4.3	(79.0–99.5)	92.9 ± 4.3	(76.7–99.4)	97.7 ± 3.9	(79.4–100)
		sCT_{air}	92.1 ± 3.3	(84.0–99.8)	92.7 ± 4.1	(76.6–99.4)	97.5 ± 4.2	(79.3–100)
		sCT_{bulk}	81.6 ± 4.0	(70.8–89.8)	81.4 ± 5.4	(64.6–88.5)	89.2 ± 7.8	(64.4–99.0)
2 mm_2%	VMAT	sCT	97.7 ± 2.2	(92.8–99.7)	93.6 ± 7.1	(73.1–99.4)	92.4 ± 13.5	(46.8–100)
		sCT_{air}	98.5 ± 1.6	(93.5–99.7)	97.1 ± 2.5	(89.5–99.3)	98.9 ± 3.4	(83.2–100)
		sCT_{bulk}	97.3 ± 2.3	(92.5–99.5)	93.2 ± 6.7	(76.5–99.7)	93.1 ± 11.2	(60.1–100)
	PBS	sCT	87.1 ± 5.4	(72.3–98.6)	89.2 ± 5.3	(71.5–97.8)	95.2 ± 5.2	(73.4–100)
		sCT_{air}	88.1 ± 4.4	(73.8–99.1)	89.2 ± 4.9	(71.4–97.9)	95.1 ± 5.6	(73.1–100)
		sCT_{bulk}	75.1 ± 4.6	(63.6–82.1)	74.5 ± 6.5	(57.4–83.6)	81.1 ± 10.4	(53.2–95.7)

Abbreviations: sd = standard deviation.

The quantitative comparison of CT and sCT images is still under discourse. Edmund and Nyholm (2017) and Johnstone *et al* (2018) underline the importance of developing common standards for the quantification of the sCT accuracy for further improvements in this field. In this study, the sCT image accuracy was evaluated by using ME and MAE metrics. The mean ME was limited (<21 HU) for all tissue classes, indicating a good fit of the sCT method in general. Nevertheless, there was a considerable variation between patients predominantly for the bone. For this volume, a mean MAE of 212 HU was calculated, even though the reported mean ME was 11 HU. This can be explained by the intensity inhomogeneity detected on the MR images mostly caused by the large imaging volume compared to other body parts such as the pelvic region. Previous studies on the prostate have reported MAE differences in the bone of 97 HU for the dual-model technique (Koivula *et al* 2016) and 134 HU for the atlas-based method (Dowling *et al* 2015). Additionally, high HU differences between the planning-CT and sCT images were detected in the ribs and in the lungs. HU differences in the ribs can be explained by their small volume, by their poor visibility on the MRI and by their position variability among all patients. Moreover, HU differences in the lungs volume can be justified by the acquisition of both planning-CT and MR images during different breathing stages. Motion compensation strategies were used during the planning-CT acquisition, by obtaining a 4D scan of a full breathing cycle, but not during the MRI acquisition. Smaller HU differences between the lungs volumes might potentially be achieved if matching breathing anatomies between MR and CT images had been evaluated. In this study, the clinical MR images were used as acquiring MRI sequences that are not included in the standard practice protocol is more difficult for children due to the stringent ethical regulations associated to this patient group. Nevertheless, no significant motion artifacts were detected in the present MRI dataset and lungs segmentation was performed directly on the MR images (figure 3). With more

Table 2. Percentage of OARs $D_{2\%}$ differences and gamma pass-rates (%) for the comparison of planning-CT and sCT/sCT_{air} doses for the patients with tumors located on the upper (Pat_{upp}s) and lower (Pat_{low}s) part of the abdomen.

			VMAT (%)				PBS (%)			
			Pat_{upp}s ($N = 9$)		Pat_{low}s ($N = 21$)		Pat_{upp}s ($N = 9$)		Pat_{low}s ($N = 21$)	
DVH	Structure		Mean	Range	Mean	Range	Mean	Range	Mean	Range
$D_{2\%}$	Kidneys	sCT	0.6	(−0.8; 1.7)	0.2	(−0.8; 1.7)	0.7	(−1.2; 5.4)	0.3	(−1.4; 2.8)
		sCT_{air}	−0.6	(−0.9; 0.1)	−0.5	(−1.3; 0.0)	0.7	(−1.2; 5.3)	0.3	(−1.4; 2.8)
	Liver	sCT	−0.1	(−0.7; 0.3)	−0.1	(−0.7; 0.4)	0.3	(−4.1; 4.0)	0.0	(−2.6; 0.4)
		sCT_{air}	−0.1	(−0.7; 0.2)	−0.4	(−0.7; 0.1)	0.0	(−4.1; 4.0)	0.1	(−2.6; 0.5)
	Spleen	sCT	0.9	(−0.1; 3.4)	−0.1	(−0.9; 0.6)	0.6	(−0.3; 3.9)	−0.1	(−2.3; 1.7)
		sCT_{air}	−0.2	(−0.9; 1.1)	−0.4	(−1.0; 0.0)	0.6	(−0.3; 3.9)	−0.1	(−2.3; 1.7)
Gamma	Threshold		Mean	Range	Mean	Range	Mean	Range	Mean	Range
2 mm_2%	10%	sCT	94.8	(92.8; 98.9)	98.7	(95.9; 99.7)	82.3	(72.3; 88.5)	88.6	(83.7; 98.6)
		sCT_{air}	96.4	(93.5; 99.5)	98.9	(96.3; 99.7)	83.3	(73.8; 88.5)	89.2	(84.6; 99.1)
	50%	sCT	85.2	(73.1; 95.5)	96.5	(86.5; 99.4)	84.5	(71.5; 92.7)	90.8	(86.9; 97.8)
		sCT_{air}	94.3	(89.5; 97.3)	97.7	(95.1; 99.3)	84.2	(71.4; 89.3)	90.3	(86.2; 97.9)
	90%	sCT	75.4	(46.8; 99.0)	97.3	(83.1; 100)	90.1	(73.4; 97.4)	96.5	(89.7; 100)
		sCT_{air}	95.6	(83.2; 100)	99.4	(94.6; 100)	89.4	(73.1; 96.2)	96.4	(87.9; 100)

focus on the MRI intensity variation and fine tuning of MRI sequences, improved results could potentially be achieved for both atlas-based segmentation and intensity conversion models.

Besides the sCT imaging comparison, another requirement for the MRI-only workflow is the practical sCT method implementation: conversion speed, robustness, usability and amount of preliminary data needed for the atlas creation or network teaching. Regarding the conversion speed, the most time-consuming task during this sCT generation method is the automatic atlas-based segmentation of bone and lungs. However, the sCT generation time is considerably fast (approximately 3 min taken fully by the automatic atlas-based segmentation step) and comparable to previous publications. The review by Johnstone *et al* (2018) presented generation times mainly under 5 min for voxel-wise methods and a larger variation from a couple of minutes to over an hour for atlas-based methods. Novel techniques based on deep learning can however provide sCT generation in the time scale of seconds (Maspero *et al* 2018). Concerning the method's usability, the sCT generation workflow was designed to be highly accessible and easily adopted by most clinical users. However, the method's commissioning presents some limitations as every user needs to validate a suitable segmentation for the bone and lungs. Regarding the amount of preliminary data needed, a considerably feasible number of patients ($N = 24$) was used for the atlas construction in this study. Nevertheless, the exact number of patients needed to assure an optimal ratio between automatic atlas-based segmentation time and accuracy still remains uncertain.

The sCT dosimetric accuracy was evaluated for both photon and proton irradiation techniques. VMAT and PBS plans were optimized on the planning-CT and re-calculated on the sCT images. No optimization of the plans on the sCT and re-calculation of the same on the planning-CT was performed. This methodology was chosen as in literature it was previously shown that the CT-sCT dose comparison was invariant with respect to the optimization method used (Koivula *et al* 2016). Results show that MRI-only photon and proton dose calculations were feasible when using the generated sCTs for pediatric patients with abdominal tumors. Mean DVH differences on the ITV between the planning-CT and the original sCT doses were smaller than 0.8% for both delivery techniques. Individual differences were up to 5% and 0.7% for the VMAT and PBS dose distributions, respectively. For the VMAT dose distributions, the ITV coverage was not met for three patients due to differences in the existence of air pockets between the planning-CT and the original sCT (figure 3). The proposed sCT generation method performed automatically a muscle HU assignment to all air cavities seen on the MRI. After delineating the air from the planning-CT and using this contour for further dose calculations on the sCT_{air}, the target coverage was restored. For photon therapy, discrepancies between planned and delivered doses generated by the presence of random air pockets in the vicinity of the ITV need to be avoided. As a result, planning strategies such as performing density override on the CT image during planning or using online daily re-planning in an MRI-guided workflow (Kontaxis *et al* 2015a, 2015b) might need to be implemented. In an MRI-guided workflow to be able to fully reproduce the patient's daily anatomy, an automatic air cavities delineation tool is essential for the investigated sCT generation method. This is particularly difficult to implement while using standard MRI sequences as both cortical bone and air have no signal on MRI. However, in literature (Johansson *et al* 2011, Edmund *et al* 2014) it has been shown that ultrashort echo time (UTE) pulse sequences can improve the contrast between bone and the surrounding air and soft-tissue enabling a rough separation between these tissues classes.

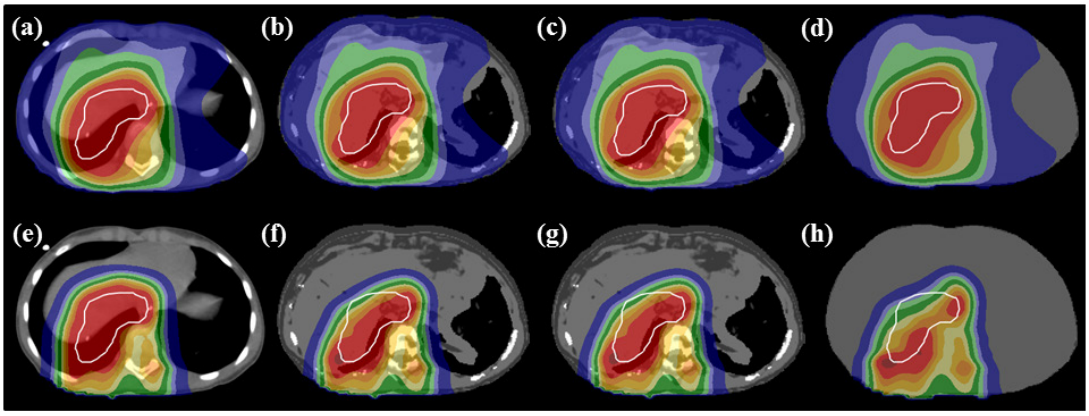

Figure 7. VMAT (top row) and PBS (bottom row) dose maps for dose distributions re-calculated on the planning-CT (a) (e), sCT (b) (f), sCT_{air} (c) (g) and sCT_{bulk} (d) (h) for one Pat_{upp}. The ITV contour is represented in white. The PD is 21.6 Gy and the 95%PD isoline is shown in red.

For PBS dose distributions, uncertainties related to the presence of random air pockets can be avoided by using posterior-oblique irradiation fields. When using this beam configuration, results show that dose differences to the planning-CT dose were similar for both original sCT and sCT_{air}.

Mean gamma pass-rates for the generated sCTs doses ranged from 92%–100% and 87%–98% for VMAT and PBS dose distributions, respectively. Gamma pass-rates results for the PBS dose distributions were lower in comparison with studies in literature evaluating the sCT proton dose calculation accuracy for patients with prostate cancer (Koivula *et al* 2016, Maspero *et al* 2017). For a 2 mm_2% criterion and 10% dose threshold, Koivula *et al* (2016) and Maspero *et al* (2017) reported a mean gamma pass-rate of 98%, in comparison with 87% in this study. Two main reasons were responsible for this lower PBS gamma pass-rate: (1) the large target size (mean 100 cc) and (2) the use of non-robust dose distributions to range uncertainty. For the patients included in this study, the ITV was extended cranio-caudally throughout the whole abdomen. As a result, sCT dose re-calculations were subjected to larger HU discrepancies detected between the planning-CT and MR images. Despite both planning-CT and MR images were acquired on the same day and under radiotherapy treatment position, the images demonstrated substantial inter-scan differences mostly regarding the lungs volume (mean DSC ~ 0.7). As a result, larger relative differences between the planning-CT and sCT doses were seen, especially for the Pat_{upp}s (figure 7). For the PBS dose distributions re-calculated on the generated sCTs, a decrease of 7 pp on the mean gamma pass-rates was calculated for the Pat_{upp}s in comparison to Pat_{low}s. In addition, PBS plans non-robust to range uncertainty were used in this study to assess the differences between the planning-CT and sCT doses in a setting more susceptible to density changes. However, protons can be more sensitive to uncertainties in CT densities and patient anatomy than photons (Lomax 1999). Robust planning is currently used in proton therapy to guarantee that the target coverage is maintained throughout the treatment by mitigating the effect of both range and set-up uncertainties. Thus, the proton dose calculation accuracy might be further improved when using a robust planning technique against both set-up and range uncertainties.

Furthermore, dose distributions were re-calculated on an homogeneous water equivalent density sCT to evaluate the added value of using the generated sCTs for the dose calculations against using the sCT_{bulk}s. Dosimetric accuracy was reduced when using the sCT_{bulk}s for the dose re-calculations, especially for the PBS dose distributions with individual dose differences to the planning-CT up to 20%.

During RTP, another aspect that should be taken into account is the MRI geometric distortions and consequently the geometric accuracy of the sCTs. Gradient non-linearity distortions are the most dominant source of MRI distortions and have been shown to be more noticeable away from the scanner isocenter (Wang *et al* 2004, Baldwin *et al* 2007). Nevertheless, Tijssen *et al* (2017) showed that geometric distortions are only limited to 0.9 mm for a spherical volume with similar dimensions to a children's abdomen (30 cm diameter). In this study, the patients' body contours between the planning-CT and sCT images were matched to reduce the influence of inter-scan differences due to patient set-up and anatomic differences on the dosimetric results (Prior *et al* 2016, Gustafsson *et al* 2017, Persson *et al* 2017). Analyzing the geometric accuracy of the generated sCTs was out of the scope of this paper, however the authors are aware that performing a match of the body contours between images might reduce the dosimetric differences seen. Future work will focus on evaluating the sCT geometric fidelity and patient position verification while using the generated sCTs for this patient group.

Similarly to the previously published dual-model technique (Korhonen *et al* 2014, Koivula *et al* 2016, 2017), the sCT generation method is robust in the absence of major artifacts and to general changes in MRI intensity levels and is suitable to be used for images acquired with different MR platforms and vendors. Improvement of

the triple-model in comparison to the dual-model technique is the expanded usability when adding lung tissue for the sCT conversion model. In contrast, it is more sensitive to variations in the MRI intensity homogeneity as there are three distinct conversion curves for which all the MRI intensities have to correspond accordingly. The sCT dosimetric accuracy for targets directly located in the lungs was not tested in this study. Nevertheless, results were presented for both Pat_{upp}s and Pat_{low}s. Despite that a feasible atlas-based segmentation of the lungs was possible when using T2w-MR images, a decrease in the dosimetric accuracy for Pat_{upp}s in comparison to Pat_{low}s was seen. For the Pat_{upp}s, these dosimetric differences might potentially be reduced if matching breathing anatomies between CT and MR images had been used. Future work should focus on improving the MRI acquisition by using motion mitigation techniques and on the development of dedicated MRI sequences for the sCT generation.

In summary, the results presented in this study are a promising step for the future clinical implementation of an MRI-only radiotherapy workflow to treat children with abdominal tumors. The employed method is able to generate sCTs with a large FOV, including the whole abdomen of the patient, which is essential for RTP. Accurate MRI-only photon dose calculations were achieved with the generated sCTs. However, the correct representation of air pockets in the bowel was found crucial. For MRI-only proton dose calculations, future research should focus in reducing anatomic differences between the CT and the generated sCTs and using robustness against range uncertainty during planning for a more realistic dose comparison.

5. Conclusions

In the present study, the feasibility of generating sCTs for children using standard T2w-MR images with a large FOV, including the whole abdomen of the patient, was evaluated. The proposed sCT generation method combined an automatic atlas-based segmentation with a triple-model technique for MRI intensity to HU values conversion for bone, lungs and soft-tissue classes. Results show that MRI-only photon and proton dose calculations for pediatric patients with abdominal tumors were feasible. Clinical implementation of the proposed method will, however, require further investigations on improving the MRI acquisition, evaluating the sCT geometric fidelity and in using robust treatment planning strategies.

ORCID iDs

Lauri Koivula https://orcid.org/0000-0001-7846-695X

References

Baldwin L N, Wachowicz K, Thomas S D, Rivest R and Fallone B G 2007 Characterization, prediction, and correction of geometric distortion in 3 T MR images *Med. Phys.* **34** 388–99

Chernak E S, Rodriguez-Antunez A, Jelden G L, Dhaliwal R S and Lavik P S 1975 The use of computed tomography for radiation therapy treatment planning *Radiology* **117** 613–4

Dinkla A M, Wolterink J M, Maspero M, Savenije M, Verhoeff J J C, Seravalli E, Isgum I, Seevinck P R and van den Berg C A T 2018 MR-only brain radiotherapy: dosimetric evaluation of synthetic CTs generated by a dilated convolutional neural network *Int. J. Radiat. Oncol. Biol. Phys.* **102** 801–12

Dowling J A *et al* 2015 Automatic substitute computed tomography generation and contouring for magnetic resonance imaging (MRI)-alone external beam radiation therapy from standard MRI sequences *Int. J. Radiat. Oncol. Biol. Phys.* **93** 1144–53

Dowling J A, Lambert J, Parker J, Salvado O, Fripp J, Capp A, Wratten C, Denham J W and Greer P B 2012 An atlas-based electron density mapping method for magnetic resonance imaging (MRI)-alone treatment planning and adaptive MRI-based prostate radiation therapy *Int. J. Radiat. Oncol. Biol. Phys.* **83** 5–11

Edmund J M and Nyholm T 2017 A review of substitute CT generation for MRI-only radiation therapy *Radiat. Oncol.* **12** 28

Edmund J M, Kjer H M, van Leemput K, Hansen R H, Andersen J A and Andreasen D 2014 A voxel-based investigation for MRI only radiotherapy of the brain using ultra short echo times *Phys. Med. Biol.* **59** 7501–19

Fredriksson A, Forsgren A and Hårdemark B 2011 Minimax optimization for handling range and setup uncertainties in proton therapy *Med. Phys.* **38** 1672–84

Guerreiro F *et al* 2017 Evaluation of a multi-atlas CT synthesis approach for MRI-only radiotherapy treatment planning *Phys. Med.* **35** 7–17

Gustafsson C, Nordstrom F, Persson E, Brynolfsson J and Olsson L E 2017 Assessment of dosimetric impact of system specific geometric distortion in an MRI only based radiotherapy workflow for prostate *Phys. Med. Biol.* **62** 2976–89

Han X 2017 MR-based synthetic CT generation using a deep convolutional neural network method *Med. Phys.* **44** 1408–19

Hsu H S, Cao Y, Huang K, Feng M and Balter J M 2013 Investigation of a method for generating synthetic CT models from MRI scans of the head and neck for radiation therapy *Phys. Med. Biol.* **58** 8419–35

Johansson A, Karlsson M and Nyholm T 2011 CT substitute derived from MRI sequences with ultrashort echo time *Med. Phys.* **38** 2708–14

Johnstone E, Wyatt J J, Henry A M, Short S C, Sebag-Montefiore D, Murray L, Kelly C G, McCallum H M and Speight R 2018 Systematic review of synthetic computed tomography generation methodologies for use in magnetic resonance imaging-only radiation therapy *Int. J. Radiat. Oncol. Biol. Phys.* **100** 199–217

Jonsson J H, Akhtari M M, Karlsson M G, Johansson A, Asklund T and Nyholm T 2015 Accuracy of inverse treatment planning on substitute CT images derived from MR data for brain lesions *Radiat. Oncol.* **10** 1–7

Koivula L J *et al* 2017 Intensity-based dual model method for generation of synthetic CT images from standard T2-weighted MR images—generalized technique for four different MR scanners *Radiother. Oncol.* **125** 411–9

Koivula L J, Wee L and Korhonen J 2016 Feasibility of MRI-only treatment planning for proton therapy in brain and prostate cancers: dose calculation accuracy in substitute CT images *Med. Phys.* **43** 4634

Kontaxis C, Bol G H, Lagendijk J J W and Raaymakers B W 2015a Towards adaptive imrt sequencing for the mr-linac *Phys. Med. Biol.* **60** 2493

Kontaxis C, Bol G H, Lagendijk J J W and Raaymakers B W 2015b A new methodology for inter- and intrafraction plan adaptation for the mr-linac *Phys. Med. Biol.* **60** 7485

Korevaar E W, van Dijk L V, Kierkels R G, Sijtsema N M, Bijl H P, Lagendijk J A and van't Veld A A 2017 Evaluation of robustness of target coverage: transition from the PTV concept to multi-scenario CTV evaluation *Proc. to the 56th Annual Meeting for the Particle Therapy Cooperative Group (PTCOG)*

Korhonen J, Kapanen M, Keyrilainen J, Seppala T and Tenhunen M 2014 A dual model HU conversion from MRI intensity values within and outside of bone segment for MRI-based radiotherapy treatment planning of prostate cancer *Med. Phys.* **41** 011704

Korsholm M E, Waring L W and Edmend J M 2014 A criterion for the reliable use of MRI-only radiotherapy *Radiat. Oncol.* **9** 16

Ladenstein R *et al* 2017 Busulfan and melphalan versus carboplatin, etoposide, and melphalan as high-dose chemotherapy for high-risk neuroblastoma (HR-NBL1/SIOPEN): an international, randomised, multi-arm, open-label, phase 3 trial *Lancet* **18** 500–14

Lagendijk J J W, Raaymakers B W, van den Berg C A T, Moerland M A, Philippens M E and van Vulpen M 2014 MR guidance in radiotherapy *Phys. Med. Biol.* **59** 349–69

Lee Y K, Bollet M, Charles-Edwards G, Flower M A, Leach M O, McNair H, Moore E, Rowbottom C and Webb S 2003 Radiotherapy treatment planning of prostate cancer using magnetic resonance imaging alone *Radiother. Oncol.* **66** 203–16

Lomax A J 1999 Intensity modulation methods for proton radiotherapy *Phys. Med. Biol.* **44** 185–205

Maspero M, Savenije M H F, Dinkla A M, Seevinck P, Intven M P W, Jurgenliemk-Schulz I M, Kerkmeijer L G W and van den Berg C A T 2018 Dose evaluation of fast synthetic-CT generation using a generative adversarial network for general pelvis MR-only radiotherapy *Phys. Med. Biol.* **63** 185001

Maspero M, van den Berg C A T, Landry G, Belka C, Parodi K, Seevinck P R, Raaymakers B W and Kurz C 2017 Feasibility of MR-only proton dose calculations for prostate cancer radiotherapy using a commercial pseudo-CT generation method *Phys. Med. Biol.* **62** 9159–76

Persson E *et al* 2017 MR-OPERA: a multi-center/multivendor validation of magnetic resonance imaging—only prostate treatment planning using synthetic computed tomography images *Int. J. Radiat. Oncol.* **99** 692–700

Prior P, Chen X, Botros M, Paulson E S, Lawton C, Erickson B and Li X A 2016 MRI-based IMRT planning for MR-linac: comparison between CT- and MRI-based plans for pancreatic and prostate cancers *Phys. Med. Biol.* **61** 3819–42

Pritchard-Jones K *et al* 2015 Omission of doxorubicin from the treatment of stage II–III, intermediate-risk Wilms' tumour (SIOP WT 2011): an open-label, non-inferiority, randomised controlled trial *Lancet* **386** 1156–64

RaySearch Laboratories 2014 RSL-D-61-217 RayPhysics 4.5 user manual Stockholm, Sweden

Sjolund J, Forsberg D, Andersson M and Knutsson H 2015 Generating patient specific pseudo-CT of the head from MR using atlas-based regression *Phys. Med. Biol.* **60** 825–39

Stanescu T, Jans H S, Pervez N, Stavrev P and Fallone B G 2008 A study on the magnetic resonance imaging (MRI)-based radiation treatment planning of intracranial lesions *Phys. Med. Biol.* **53** 3579–93

Tenhunen M, Korhonen J, Kapanen M, Seppala T, Koivula L, Collan J, Saarilahti K and Visapaa H 2018 MRI-only based radiation therapy of prostate cancer: workflow and early clinical experience *Acta Oncol.* **28** 1–6

Tijssen R H N, Crijns S P M, Bluemink S S, Hacket S S, de Vries J H W, Kruiskamp M J, Philippens M E P, Lagendijk J J W and Raaymakers B W 2017 Comprehensive MRI acceptance testing & commissioning of a 1.5T MR-linac: guidelines and initial results *Radiother. Oncol.* **123** 130–1

Tustison N J, Avants B B, Cook P A, Zheng Y, Egan A, Yushkevich P A and Gee J C 2010 N4ITK: improved N3 bias correction *IEEE Trans. Med. Imaging* **29** 1310–20

Uh J, Merchant T E, Li Y, Li X and Hua C 2014 MRI-based treatment planning with pseudo CT generated through atlas registration *Med. Phys.* **41** 051711

Wang D, Strugnell W, Cowin G, Doddrell D M and Slaughter R 2004 Geometric distortion in clinical MRI systems part I: evaluation using a 3D phantom *Magn. Reson. Imaging* **22** 1211–21